

Nanotheranostics of Pre-Stenotic Vessels By Target Touch-On Signaling of Peptide Navigator

Seung Eun Yu, Seyong Chung, Hyun-Su Ha, Dae-Hyun Kim, Sewoom Baek, Tae Young Kim, Songhyun Lee, Hyo-Jin Yoon, Soon Won Chung, Jung Bok Lee, Young Min Shin, Hye-Seon Kim, Si Young Kim, Joon-Sang Park, Chang-Soo Kim,* and Hak-Joon Sung*

Navigation of nanoparticles to target sites of blood flow disturbance markedly upgrades the diagnostic paradigm in vascular medicine. The theranostic treatment of pre-stenotic vessels can prevent the irreversible occlusion process effectively. Here, these nanotheranostic functions are established by displaying CDK9(cyclin-dependent kinase 9)-targeting peptide (P.) onto nanovesicles (NV) and liposomes using the navigation function and subsequent binding-on signaling of P. as a game-changer. When rabbit vessels are allografted with injecting contrast-loaded P. liposomes, the case-dependent stenotic degree after 2–6 weeks can be diagnosed accurately within 2–4 days via computed tomography imaging with cross-validation in a mouse model of partial carotid ligation. Furthermore, the anti-CDK9 signaling of P. NV is activated post-targeting and effectively prevents vascular stenosis by suppressing inflammation and lipotoxicity in the vessels, serum, and/or liver. CDK9 targeting is confirmed using computer, in vitro, and in vivo models. This study demonstrates an unprecedented nanotheranostic function for future clinical applications.

the body circulation to activate anti-stenotic effects (therapy). The earliest stenotic signals should be detected because vascular stenosis cascades irreversibly.^[1,2] Thus, once a vessel starts to exhibit well-known molecular events such as endothelial expression of adhesion molecules to recruit inflammatory cells,^[2–4] stenosis is impossible to stop or prevent despite tremendous therapeutic efforts.^[5] Over the past several decades, blood flow disturbance has been recognized as one of the earliest events^[6,7] to trigger the stenotic process, indicating its qualification as a theranostic target. Moreover, immediate therapeutic activation by touching a target represents one of the most effective operation mechanisms that diagnostic power can synergize, which inevitably requires a target binding-mediated anti-stenotic signaling.


1. Introduction

A navigator recognizes a target site and provides directional guidance to reach the site through complex routes, thereby helping to achieve a goal. Likewise, the ideal vascular nanotheranostics should be operated by detecting the earliest stenotic signal (diagnostics) and thereby navigate the stenosis-initiating site through

Although blood flow disturbance is considered, the nature of targeting relies on finding a molecular address that can guide targeting erroneously to more than one place as often seen in a navigation system. In the body, this error can be reversely applied to approach the concept of multi-organ therapy. Together, this study validated these breakthrough concepts of nanotheranostics through computational modeling, preclinical

S. E. Yu, S. Chung, H. S. Ha, S. W. Baek, T. Y. Kim, S. Lee, H. J. Yoon, Y. M. Shin, H. S. Kim, S. Y. Kim, C. S. Kim, H. J. Sung
Department of Medical Engineering
Yonsei University College of Medicine
50-1 Yonsei-ro, Seodaemun-gu, Seoul 03722, Republic of Korea
E-mail: ckim4@numais.com; hj72sung@yuhs.ac

D. H. Kim
Department of Veterinary Surgery
College of Veterinary Medicine
Chungnam National University
Daejeon 34134, South Korea

 The ORCID identification number(s) for the author(s) of this article can be found under <https://doi.org/10.1002/adfm.202110368>.

© 2021 The Authors. Advanced Functional Materials published by Wiley-VCH GmbH. This is an open access article under the terms of the Creative Commons Attribution-NonCommercial-NoDerivs License, which permits use and distribution in any medium, provided the original work is properly cited, the use is non-commercial and no modifications or adaptations are made.

S. W. Chung
Department of Plastic Surgery
Korea University Guro Hospital
Seoul 08308, Republic of Korea

J. B. Lee
Department of Biological Science
Sookmyung Women's University
Seoul 04314, Republic of Korea

J. S. Park
Department of Computer Engineering
Hongik University
Seoul 04066, Republic of Korea

C. S. Kim
Numais Co., Ltd., Korea
Seoul 04799, Republic of Korea

DOI: 10.1002/adfm.202110368

models, and a flow model of human cells using the following game-changers. First, a peptide with a sequence of ACTPS-FSKIC (P.) was displayed on the liposome as a navigator to guide targeting sites of disturbed flow to upgrade the diagnostic power.^[8] Indeed, applying P. liposomes on days 2–4 after vascular surgery enabled precise prediction of vascular stenosis after 2–6 weeks.

Second, as a molecular address, cyclin-dependent kinase 9 (CDK9) was identified to bind P. because the expression of CDK9 increased markedly at vascular sites of blood flow disturbance with co-incidental overexpression in the liver, thereby exerting synergistic therapeutic efforts to suppress stenosis and lipotoxicity in multiple organs. As a factor of the positive transcription elongation factor b (P-TEFb) complex,^[9] CDK9 expression increased in patients with coronary artery atherosclerosis,^[10] and dysregulation of CDK9 functions has been associated with anti-stenotic effects by suppressing intimal hyperplasia^[11] and inflammation^[9,12–15] in addition to liver therapy.^[16]

As an additional justification, P. was displayed onto nanovesicle (NV) from tonsil-derived mesenchymal stem cells (TMSCs) to examine anti-stenotic signaling compared to liposome because NV carry a miRNA profile^[17] absent in liposomes, and the miRNA profiles represent both therapeutic and side effects as seen in any drug. Computed tomography (CT) imaging was applied by loading Active Ingredient contrast into P. liposome because CT is a cheaper and faster imaging modality compared to magnetic resonance imaging and PET-CT,^[18] allowing more patients to get cost and speed benefits. However, even though a contrast agent is used as required, its low sensitivity, short signal period (<24 h), and side organ toxicity should be overcome using nanoparticles.^[18,19] Addressing these issues by targeting the efficiency of P. NV is another breakthrough of this study.

In summary, this study focused on the key nanotheranostic roles of P. in leading diagnostic navigation to disturbed flow sites together with subsequent activation of touch-on therapeutic signaling (Figure 1). P. sensed blood flow disturbance efficiently and bound to CDK9 upon overexpression in the context, thereby suppressing CDK9-associated stenotic actions. Since P. needed cargos to carry over diagnostic and therapeutic contents, the Active Ingredient contrast was loaded into P. liposomes for CT imaging, while P. NV was used because the internal miRNA profile like any other drugs could exert both therapeutic and side effects. Their nanotheranostic functions were validated in preclinical rabbit allograft and mouse partial carotid ligation (PCL) and an in vitro flow model with human cells. As an unprecedented example, early diagnosis and therapeutic prevention of stenosis development in vessels using the nanotheranostic toolbox were demonstrated.

2. Results

2.1. Early Prediction of Stenotic Vessel using P

First, to produce the P. nanoparticles, liposomes were produced by rapid injection of a lipid mixture with a CT imaging agent, and NV were produced through a series of filtering of TMSCs for diagnostic and therapy, respectively (Figure S1a, Supporting Information). Then, P. was conjugated with PEG-

DSPE (1,2-distearoyl-sn-glycero-3-phosphoethanolamine-N-[carboxy(polyethylene glycol)-2000]) and displayed through electroporation on liposomes and NV. These particles exhibited intact circular morphologies and 100–150 nm size distribution with the average diameters of 106.84 ± 4.38 nm (P. NV) and 117.34 ± 4.59 nm (P. liposome) in transmission electron microscopy analyses (Figure S1b, Supporting Information). After the entire production process, NV maintained expression of the exosome (CD9 and CD63) and TMSC (actin) markers before (NV) and after P. display (P. NV and scramble P. NV) in western blot analyses (Figure S1c, Supporting Information), indicating the promising potential of NV to carry over the TMSC content like exosomes. As a key element for the navigation function, displaying P. onto NV was also confirmed in a step-by-step manner from P.-PEG-DSPE to P.-PEG-DSPE-NV in Fourier transform infrared (FTIR) analyses (Figure S1d, Supporting Information). In addition, a sufficient diagnostic signal was produced by loading 80 mg iodide/mL into liposomes as determined by X-ray imaging (Figure S1e, Supporting Information).

As a punchline example, P. liposomes containing the Active Ingredient contrast were used to predict the degree of stenosis through early diagnostic analyses of the CT signals from sites of blood flow disturbance (Figure 2a). As a blind test with no surgical control of the vascular patency and result reproducibility, the case-by-case prognosis after allografting of rabbit carotid artery (day 0) was approached by immediately conducting ultrasound imaging of blood flow direction and speed (day 0) and then injecting P. liposome (+ contrast) with CT imaging (day 2–4). Finally, to validate the diagnostic power of P. liposomes seen on CT imaging, stenotic severance was characterized by ultrasound imaging and pathological analyses (week 2–6). The experimental goal was to test the prediction capability of P. liposome (+ contrast) within the context of no foreseeable outcomes. As a result, the CT signal increased significantly in Graft over Intact for 48 h post P. liposome injection, indicating cumulative targeting of P. liposome to disturbed flow sites around the allograft (Figure 2b,c). Since most CT contrasts are cleared off from the body within 24 h,^[18,19] the incremental CT signals during 48 h indicate that efficient targeting could improve the diagnostic power.

Both desirable (top) and undesirable (bottom) prognostic cases showed a similar maximum flow velocity initially (day 0) (Figure 2d). However, the undesirable case exhibited more than a twofold increase in the diagnostic CT signal of Graft over Intact upon diagnosis compared to the desirable case (day 2–4). This early diagnostic result accurately predicted the later stenosis degree: i) the undesirable case exhibited more than five times decreases from 0.6 to 0.1 m s^{-1} in the maximum flow velocity with occlusive lumen even at week 2 post-surgery compared to the degree of decreased maximum flow velocity from 0.6 to 0.5 m s^{-1} in the desirable case with the clear flow patency. ii) In contrast, the desirable case maintained the maximum flow velocity with an open lumen for six weeks. This result represents a paradigm shift in vascular medicine because current diagnostic methods utilize stenotic structural and flow indicators seen after vascular remodeling started already. Thus, besides delaying the process using stent and drug there is no means to stop the pathological momentum toward lumen occlusion. Early diagnosis by targeting sites of blood flow disturbance served as a game-changer in preventing stenosis even before reaching a stage to stop the pathological momentum.

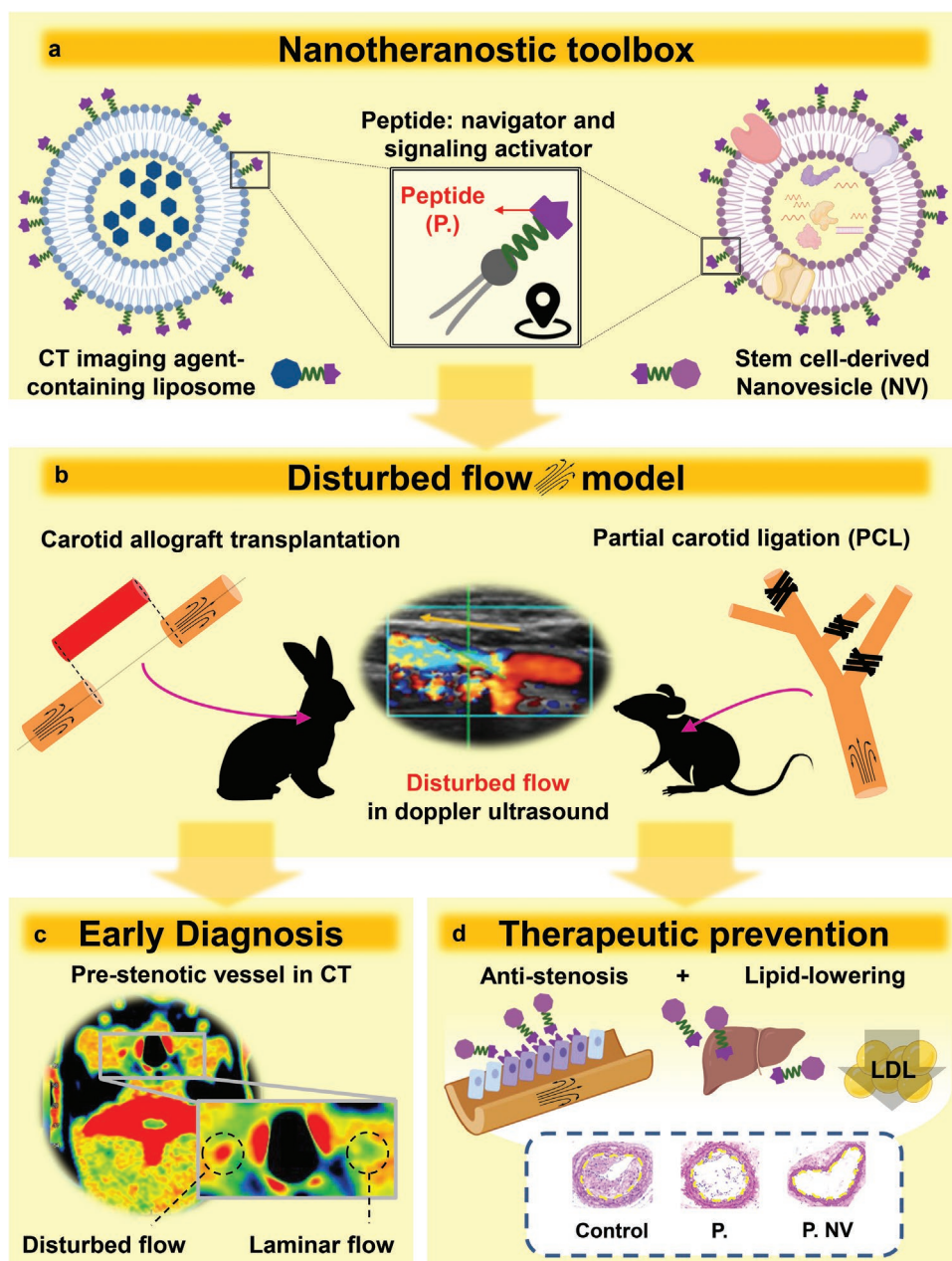


Figure 1. Disturbed flow-sensing P. as a key factor of nanotheranostic toolbox to simultaneously operate vascular targeting and anti-stenotic signaling. CT contrast loading to P. liposome; and stem cell-derived P. NV supports the nanotheranostic function as validated in rabbit allograft and mouse PCL models. The nanotheranostic function enables early diagnosis and therapeutic prevention of stenosis development in vessels.

The diagnostic efficiency of P. liposomes with contrasts was cross-validated by injection through the tail vein of each mouse after PCL surgery. After establishing the PCL model for blood flow disturbances (day 0) (Figure S2a, Supporting Information) as reported previously,^[20] mice underwent ultrasound imaging to characterize flow disturbance (day 3) and western diet until P. NV or P. liposome injection through the tail vein (day 30). Diagnostic CT imaging was performed for the next three days to predict the degree of stenosis as determined by pathology (day 60). The ligation points of the carotid artery were confirmed by 3D reconstruction of the CT images (Figure S2b, Supporting Infor-

mation), followed by validation of blood flow disturbance by ultrasound imaging (Figure S2c, Supporting Information). Indeed, P. guided liposomes targeted the site of disturbed blood flow, as evidenced by the increased CT signal in the PCL side compared to the intact side for 48 h (Figure 2e,f). This targeting efficiency was double-checked using P. NV and scramble P. NV with IVIS imaging (Figure S2d,e, Supporting Information). Together with the results, this P. liposome diagnosis represents an unprecedented, universal tool that enables circulation navigation to detect pathological vascular remodeling accompanying blood flow disturbance, as validated in both rabbit and mouse models.

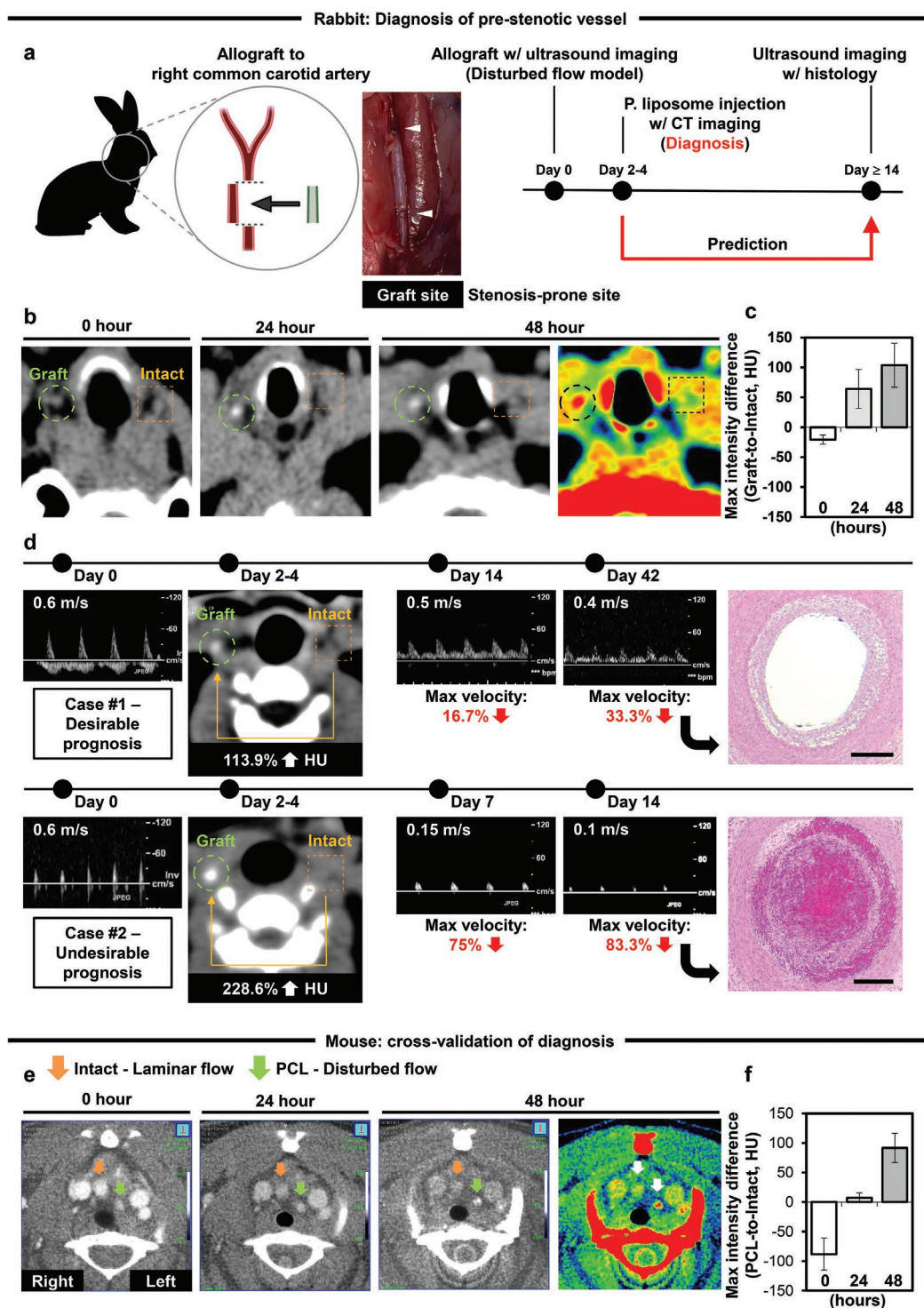


Figure 2. Prediction of progressive stenotic severance by diagnosing the degree of disturbed blood flow early after vascular surgery in preclinical cases. a) As a stenosis-prone model ($N = 3$), each rabbit underwent allograft into the right common carotid (arrowheads: sutured sites) with ultrasound imaging of blood flow direction and speed (day 0). Then, diagnosis of the disturbed flow degree was conducted by ear vein injection of P. liposome containing contrast agents with CT imaging (day 2–4). Finally, the stenotic severance was characterized by ultrasound imaging and pathology (week 2–6). b) The CT signal significantly increased in Graft over Intact for 48 h, validating accumulative targeting of P. liposome to disturbed flow sites around the allograft c) as confirmed by quantitative analyses of the max intensity difference between Graft and Intact (HU: Hounsfield units). d) Despite the similar max flow velocity (day 0), compared to the desirable case (top), the CT signal of Graft over Intact increased more than twice in the undesirable case (bottom) upon diagnosis (day 2–4), resulting in over five times decrease in the max flow velocity with an occlusive lumen in the histology (week 2–6, Scale bar = 200 μ m). e) The diagnostic efficiency of P. liposome with contrasts was cross-validated by injecting through tail vein of each PCL mouse ($N = 3$). f) The PCL side increased the CT signals for 48 h as opposed to the Intact side as confirmed by quantitative analyses of the max intensity difference between PCL and Intact. Data = mean \pm SEM.

2.2. Site-Specific Operation toward Therapeutic Prevention of Vascular Diseases

Next, the therapeutic efficiency and efficacy of P. NV upon reaching the target sites were examined, focusing on site-specific suppression of vascular stenosis in synergistic effects to lower lipid deposition (Figure 3). When the PCL model with apolipoprotein E knockout (ApoE KO) mice was examined (Figure S2a, Supporting Information) injection of saline (vehicle control) and scramble P. NV led to nearly complete occlusion of the lumen in the PCL side in contrast to the open lumen of the intact side in hematoxylin and eosin (H&E) analyses (Figure 3a; Figure S3a,b, Supporting Information), validating the stenosis model. However, injection of P. NV or P. liposome significantly reduced the formation of intimal hyperplasia to levels comparable to that of daily oral administration of Active Ingredient, indicating a promising potential of P. for suppressing vascular stenosis. This anti-stenosis effect of P. was also evidenced by the suppression of endothelial recruiting (vascular cell adhesion protein 1 [VCAM1]) of monocytes (CD68) on the PCL side compared to saline, and scramble P. NV in analyses of protein marker expression (Figure 3b; Figure S3c, Supporting Information). Notably, while monocyte invasion (CD68) was suppressed by P. liposome to the level of P. NV, NV helped P. to reduce VCAM1 expression compared to P. liposome, indicating the synergistic effect of internal miRNA. Since systemic lipid accumulation plays a key causative role in inducing vascular stenosis,^[21,22] the lipid-lowering effects of P. NV and P. liposomes were determined by focusing on the liver, blood, and aorta as sites of lipid metabolism, transport, and natural deposition, respectively. When the liver was examined in comparison to the saline group, P. targeting resulted in a significant reduction in lipid accumulation and oxidative lipo-toxicity (Figure 3c) in alignment with increased gene expression of low density lipoprotein (LDL)-lowering markers (LDL receptor, peroxisome proliferator-activated receptor γ [PPAR γ], and sterol regulatory element-binding protein 1/2 [SREBP1/2]) (Figure 3d). As a checkpoint of possible side effects, the P. NV treatment resulted in maintenance of normal liver functions to the levels of saline treatment when key biochemical parameters (Bilirubin, AST, ALT, LDH, and ALP) were assessed using the mouse blood (Figure S4a, Supporting Information). These results were clearly supported by no significant changes of the parameters post NV treatment for 14 days in rabbit (Figure S4b, Supporting Information). In the blood, the lipid-lowering effects of P. targeting were also clearly evidenced as the levels of the lipid accumulation indicators (LDL, total cholesterol, and triglyceride) decreased significantly after injection of P. NV and P. liposomes compared to saline injection (Figure 3e). Similarly, P. targeting also reduced inflammatory IL-6 production, most likely due to screening of CDK9 function upon P. binding in the liver (Figure 3f), and the lipid-lowering effects were validated by marked decreases of lipid accumulation in the aorta (Figure 3g). As mentioned above, synergistic therapeutic effects with NV containing miRNA contents were observed in the lipid-lowering effects of P. NV compared to P. liposomes. Nonetheless, these results indicate clear benefits of P.-mediated multi-organ targeting including flow disturbance sites and the liver, which is similar to the reverse use of navigating error to target more than one address.

This multi-organ targeting of P. was operated by initial targeting to vessels (0 h), followed by incremental accumulation at main waypoints, such as the liver and spleen (24–48 h) as tracked by P. liposome injection with CT imaging in the rabbit allograft model (Figure 4a,b). Similar results were confirmed using the mouse PCL model (Figure 4c,d). Next, in the mouse PCL model, IVIS signals of P. NV group (NV with pegylated P.) were sequentially compared to No P. group (NV with pegylation) and scramble P. group (NV with pegylated scramble P.). Even after 48 h, P. navigator still directed the targeting of NV and liposomes to the liver and/or spleen more effectively than the corresponding No P. control (Figure 4e,f), while P. liposomes targeting the spleen appeared to be unclear. As a validation of the P. navigator operation mechanism, scramble P., in contrast to P, did not guide NV targeting to the vessel point of blood flow disturbance. Instead, scramble P. NV continuously accumulated in the liver more dominantly with a clearer IVIS signal in the spleen than the P.-displaying groups, as examined throughout the whole mouse body and in the harvested organs (Figure 4g,h). The results present the possibility of multi-organ therapies using single-molecular targeting through body circulation. Because a disease occurs due to mis-signaling transfer or abnormal collaboration among organs in the body, the current approach serves as a foundation for a breakthrough strategy considering multi-organ collaboration for site-specific prevention of vascular diseases.

2.3. CDK9 as a Key Player of P. Navigation and Anti-Stenotic Signaling

Since P. appeared to target CDK9, P. binding to P-TEFb (CDK9 complex) was presented in the 3D computational modeling with confirmation by the best docking score (Figure 5a). In ApoE KO mice fed a western diet after PCL surgery, CDK9 expression increased under disturbed flow compared to laminar flow (Figure 5b; Figure S5a, Supporting Information). This result was double-checked by en face staining of the curved arch site under disturbed flow in the aorta compared to the linear site under laminar flow (Figure 5c) by comparing the aligned (laminar flow) and non-aligned (disturbed flow) cell populations (Figure S5b, Supporting Information). In the in vitro flow model, hAECs were seeded (day 0) and then subjected to disturbed or laminar flow (day 2) by treating NV or liposomes (day 3) until endpoint confocal imaging (day 4) (Figure S5c, Supporting Information), followed by confirmation of aligned (laminar flow) versus non-aligned (disturbed flow) cell populations (Figure S5d, Supporting Information). Under disturbed flow, more binding between P. and CDK9 was confirmed by immunoprecipitation than the laminar flow condition (Figure 5d; Figure S5e, Supporting Information), likely due to the increased expression of CDK9 compared to the laminar flow condition (Figure S5f, Supporting Information). When the kinase activity of CDK9 upon P. binding was determined using a luminescent assay, as an indication of incremental kinase inhibition, the remained ATP amount continuously increased as the P. concentration was increased from 0 to 90 μmol (Figure 5e). This result was confirmed by most co-localization of P. with CDK9 under disturbed flow among the test groups (Figure 5f; Figure S5g, Supporting Information).

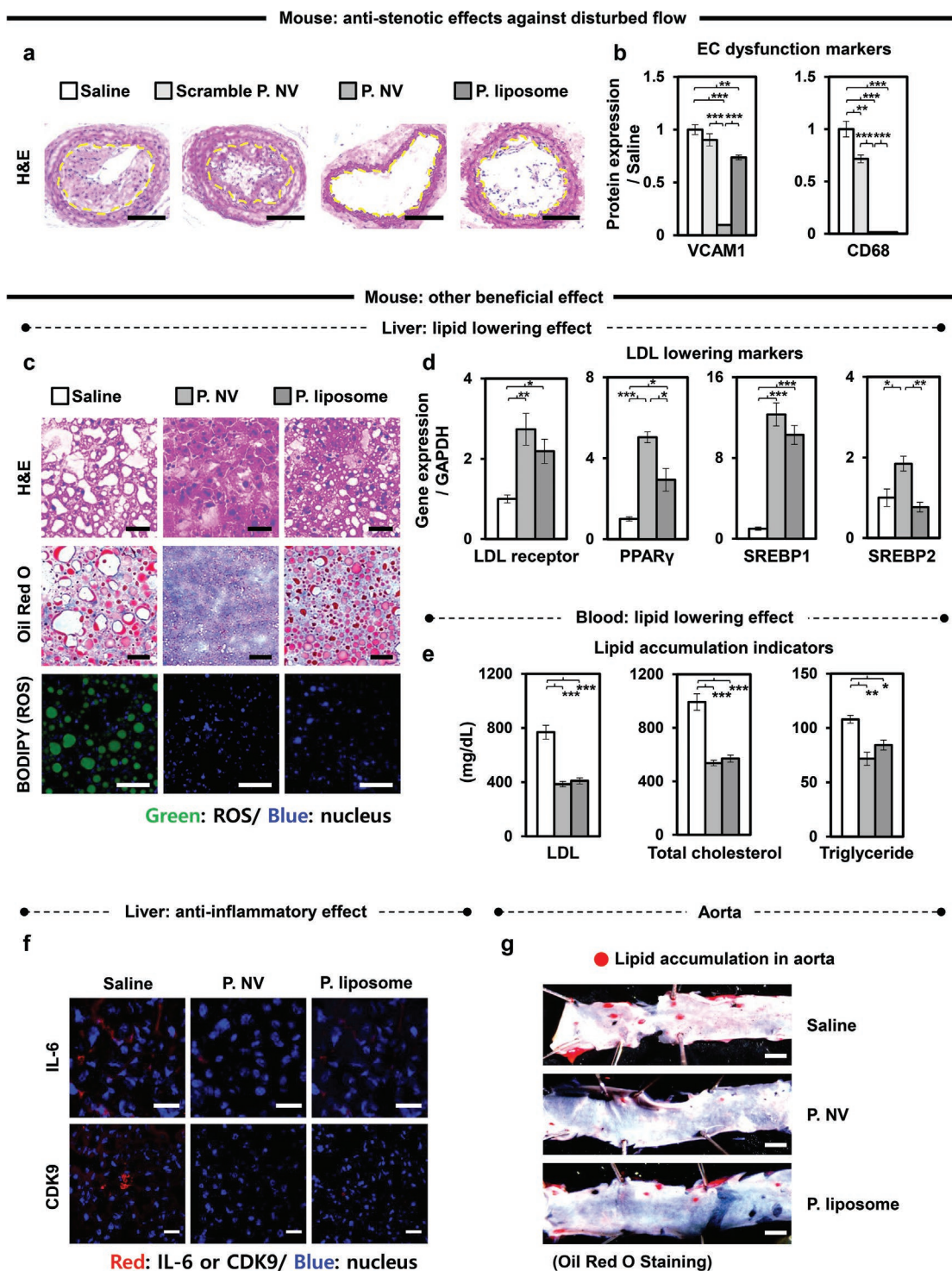


Figure 3. Synergistic anti-stenotic therapy by P. targeting to multi-organs. After PCL surgery (day 0), ApoE KO mice underwent western diet from day 3 to 30, followed by tail vein injection of test groups for the next 30 days ($N = 3$). Upon sacrifice, a) H&E staining was conducted to determine the neointima formation of ligated vessels (Yellow line: neointima boundary/Scale bar = 200 μm) with b) quantitative analyses of marker protein expression to determine inflammatory cell adhesion (VCAM1) and monocyte invasion (CD68). In order to examine lipid-lowering effects upon the synergistic multi-organ targeting, the liver was examined c) histologically (Scale bar = 25 μm) by (top) H&E staining (white circle: lipid droplet), (middle) Oil Red O staining (red: lipid), and (bottom) BODIPY staining (green: ROS/blue: nucleus), d) gene expression of lipid lowering factors (LDL receptor, PPAR γ , SREBP1, and SREBP2), e) lipid contents (LDL, total cholesterol, and triglyceride) in blood, as supported by f) (top) suppression of inflammatory cytokine production (red: IL-6) upon (bottom) screening CDK9 function (red). Scale bar = 25 μm . The synergistic actions of multi-organ targeting reduced systemic lipid accumulation in the vascular system as indicated by g) en face Oil Red O staining of aorta (red: lipid). Scale bar = 100 μm . Data = mean \pm SEM. * $p < 0.05$; ** $p < 0.01$; and *** $p < 0.001$ between lined groups.

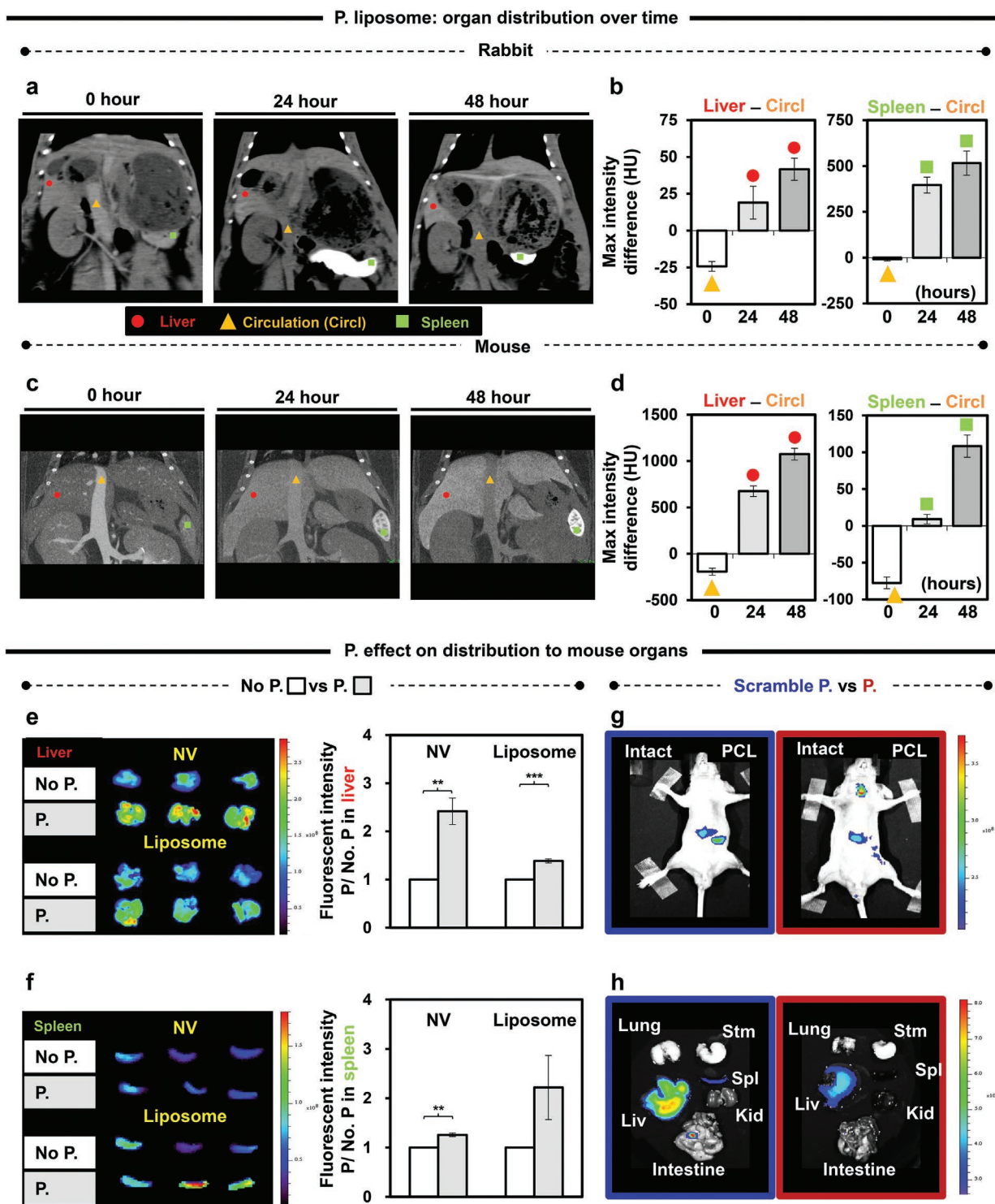


Figure 4. Operation of P. navigator by increased vessel targeting compared to waypoint accumulation. P. liposome containing contrast was circulated to target more initially (0 h) post-injection in CT imaging. However, accumulation into the waypoint organs (liver and spleen) was increased gradually over time during 48 h in a) the rabbit model of carotid allograft with b) quantitative analysis of the max intensity difference in HU (liver or spleen—circulation). These results were supported by c) CT imaging of the mouse PCL model d) with the same quantitative analysis. Then, the IVIS signals were analyzed at 48 h post-injection to the mouse PCL model. Compared to No P. groups, P. navigator still guided the targeting of NV and liposome to e) the liver and f) the spleen more effectively. In contrast, the guiding effect on liposome targeting to the spleen was attenuated. Data = mean ± SEM. ^{**}*p* < 0.01, and ^{***}*p* < 0.001 between lined groups. As a validation of the operation mechanism of P. navigator, the scramble P. did not increase NV targeting to the vessel point of blood flow disturbance. As a result, scramble P. NV was continuously accumulated in the liver more dominantly with the clearer IVIS signal in the spleen, compared to the P.-displaying groups, as examined g) throughout the whole mouse body and h) in the harvested organs (stm: stomach, liv: liver, spl: spleen, kid: kidney).

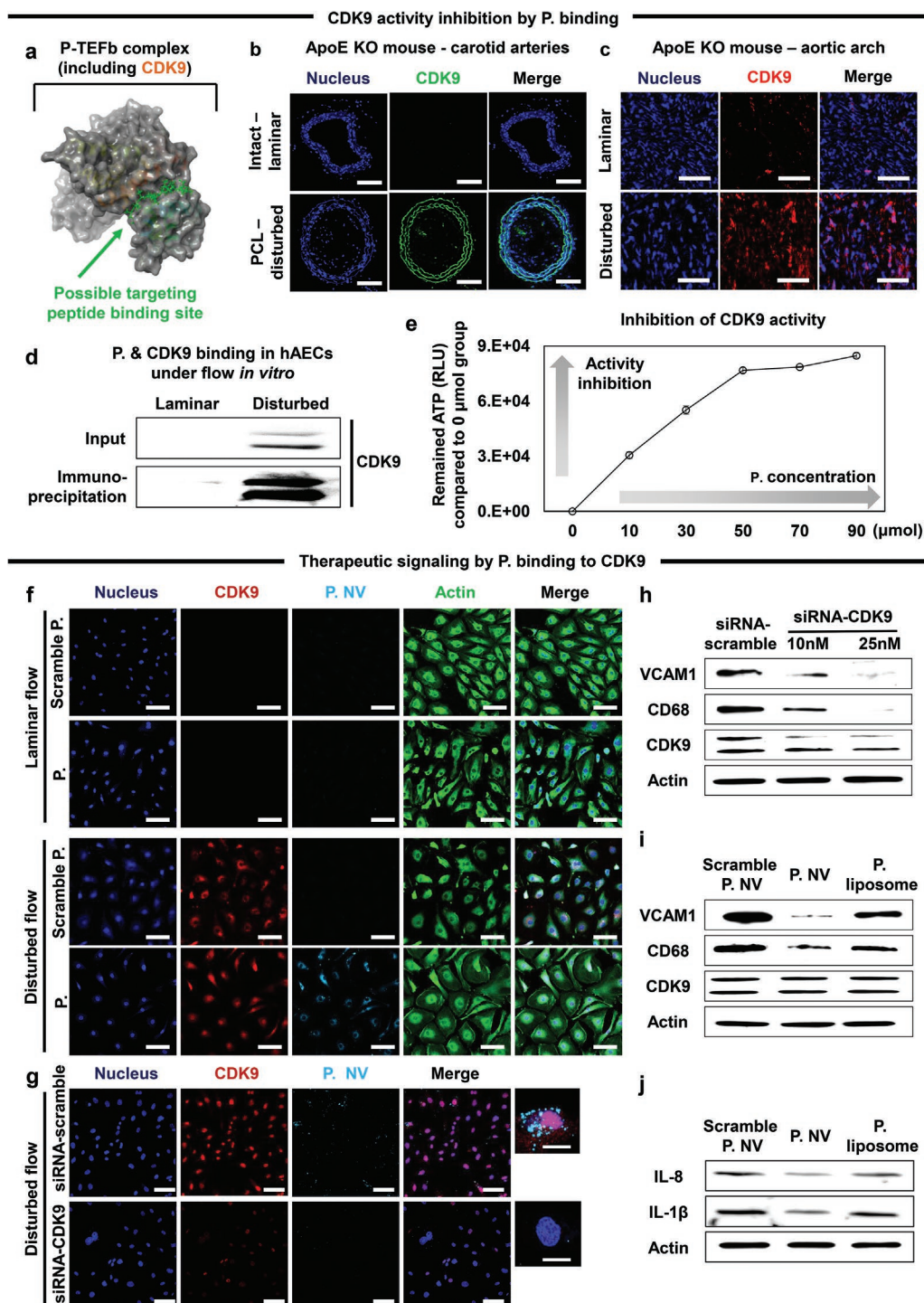


Figure 5. CDK9 as a touch button of P. targeting to turn on anti-stenotic signaling. a) P. binding (ocher) to P-TEFb complex was 3D-modeled following the best docking score. b) In ApoE KO mice with western diet post PCL surgery ($N = 3$), abundant CDK9 expression (green) under disturbed flow was validated by immunostaining compared to the laminar flow. Scale bar = 200 μ m. c) The natural disturbed flow site in aortic arch also showed abundant CDK9 expression (red) compared to laminar flow site. Scale bar = 50 μ m. When hAEC were exposed to laminar versus disturbed flow ($N = 3$), d) binding between P. and CDK9 was determined by immunoprecipitation. e) Inhibition of the CDK9 activity by P. binding was determined in response to the incremental P. concentration ($N = 3$). Data = mean \pm SEM. f) Compared to the laminar flow, disturbed flow induced CDK9 expression (red) markedly and consequent P. NV co-localization (targeting: cyan) in hAECs by immunostaining, which was not seen when the scramble P. was used in both conditions. Scale bar = 100 or 20 μ m (magnified). In western blot, h) expression of VCAM1 and CD68 in addition to CDK 9 was reduced markedly as the dose of siRNA-CDK9 increased compared to the use siRNA-scramble. i) While preserving CDK9 expression, the same effect was exerted by P. NV in contrast to scramble P. NV and P. liposome, j) in alignment with the expression of IL-8 and IL-1 β .

Even under disturbed flow, knockdown of CDK9 by siRNA decreased the co-localization with P. significantly compared to the use of siRNA-scramble, indicating the need for CDK9 to bind with P. (Figure 5g; Figure S5h, Supporting Information). When analyzed by qRT-PCR, disturbed flow induced marker gene expression of inflammatory cell recruiting (VCAM1, ICAM1, and E-selectin) (Figure S6a, Supporting Information), indicating the need for anti-stenotic action. However, the incremental knockdown of CDK9 by increasing the siRNA concentration appeared to suppress recruitment (VCAM1) of monocytes (CD68) when examined by western blot, compared to siRNA-scramble (Figure 5h; Figure S6b, Supporting Information). The same anti-stenotic effect as the knockdown of CDK9 was exerted most efficiently by P. NV treatment, while CDK9 expression was preserved at the protein level among the test groups (Figure 5i). This result was supported by the reduced gene expression of VCAM1, ICAM1, and E-selectin upon treatment with P. NV or P. liposome (Figure S6c, Supporting Information), in alignment with significant decreases in protein marker expression for endothelial recruitment (VCAM1) of monocytes (CD68) (Figure S6d, Supporting Information). Lastly, P. targeting reduced cytokine production (IL-8 and IL-1 β) significantly at the protein levels while the effect of P. liposome to reduce IL-8 expression appeared to be unclear due to the absence of internal therapeutics in contrast to the miRNA of P. NV. (Figure 5j; Figure S6d, Supporting Information).

3. Conclusion

The current study has a high impact on the field of vascular medicine because of the following significances. First, early diagnosis enabled accurate prediction of vascular stenosis that occurred even several weeks later. This was possible by P. navigator targeting the sites of blood flow disturbance, which occurs even before pathological remodeling of the vascular structure appears, indicating the possibility of therapeutic prevention. Even the most advanced approach to diagnosing vascular diseases relies on abnormal indicators of vascular structure and blood flow. Hence, the current method represents a paradigm shift toward future medicine. Second, the site-specific therapeutic prevention of vascular disease was enabled by multi-organ targeting with the reverse strategic use of erroneous navigating to multi-addresses. Molecular signaling cannot be limited to a single spot or one organ in the body. If the same signaling is collaboratively operated from multiple spots, the power is inevitably intensified. The present study applied this strategy to synergize anti-stenotic signaling in vascular sites in cooperation with lipid-lowering effects in the liver, which has never been reported in the field.

Lastly, single molecular targeting (i.e., binding P. to CDK9) enabled both early diagnosis and site-specific therapeutic prevention of vascular stenosis. Here, CDK9 was overexpressed in response to blood flow disturbances and thus served as a target address in multiple organs. Moreover, screening CDK9 expression by P. binding operated a series of mechanistic actions from suppression of CDK9 signaling to anti-stenotic action and lipid-lowering effects. Since this strategy can be used to treat other diseases, a broad impact can be provided to other fields of biotechnology and medicine.^[23] Because CDK9 is expressed

mainly inside cells, an exact mechanism to lead targeting and therapeutic activation of P. NV from blood circulation should be studied further. Atherosclerotic patients exhibited significantly higher levels of serum CDK9 compared to healthy patients,^[10] and extracellular deposition of CDK9 was seen in our result (Figure 5b), indicating a possibility of CDK9 secretion from cells. Furthermore, although CDK9 was expressed in both cytosol and nucleus, the P. NV signals were seen in only cytosol areas (Figure 5f,g). Therefore, P. NV binding to CDK9 might occur in the extracellular space and led a therapeutic action to suppress inflammatory activation as reported previously.^[15] Then, some of the P. NV-CDK9 complex could be internalized into cells to potentiate the therapeutic power. Also, the spleen targeting of P. suggests a follow-up study in the future, since the spleen is the main site of massive monocyte gathering.^[24,25] Thus, this benefit may provide another route to increase the duration of the nanotheranostic P. effect through a cargo change of nanoparticles into monocytes in the body.

4. Experimental Section

Liposome Production: Liposomes were produced by a rapid injection method. First, 1,2-dipalmitoyl-sn-glycero-3-phosphocholine (DPPC; 850355P, Sigma-Aldrich, MO, USA), cholesterol (C8667, Sigma-Aldrich), and 1,2-distearoyl-sn-glycero-3-phosphoethanolamine-N-[methoxy(polyethylene glycol)-2000] (DSPE-mPEG; 880120P, Sigma-Aldrich) were dissolved (55:40:5 molar ratio) in ethanol (E7023, Sigma-Aldrich) at 72 °C to be the final concentration of 200 mmol L⁻¹. Then, this mixture was rapidly injected into the same volume of Active Ingredient (CT contrast, 320 mg iodide/mL, GE Healthcare, IL, USA) under vigorous stirring (500 rpm) at 72 °C. The rapid injection was performed using a 20-gauge needle (Koreavaccine, Seoul, Republic of Korea) coupled to a plastic syringe (Resteck, PA, USA), followed by vigorous stirring for 5 min and the addition of Active Ingredient in a quadruple volume.

After stirring more for 15 min at room temperature, the mixture was extruded through three filters in the order of drain disc (PETEDD9025, Sterlitech, WA, USA), 0.1 μ m membrane filter (PCT019030, Sterlitech), and drain disc again at 25 mL min⁻¹ using an extruder (GOE-1000 mL, Genizer, CA, USA), and peristaltic pump (BT100L, Lead Fluid Technology, Hebei, China). Extrusion was repeated seven times, and the total volume was dialyzed using a 12–14 kDa molecular weight cutoff (MWCO) membrane (132678T, Repligen, MA, USA) against phosphate-buffered saline (PBS; LB004-02, Welgene, Seoul, Republic of Korea) for 24 h to remove free Active Ingredient. Liposomes containing Active Ingredient were acquired by centrifugation at 14 000 rpm for 1 h and used for CT imaging. Active Ingredient-free liposomes were produced by skipping the Active Ingredient mixing step for use in other experiments.

NV Production: TMSCs were isolated from young human donors (\approx 10 years old) who had undergone tonsillectomy. The study was approved by the Institutional Review Board (IRB) of Yonsei University College of Medicine (IRB No. 4-2019-1260) and conducted with parents after written consent was obtained from their guardians. After washing three times, tonsil tissues were mechanically cut and enzymatically dissociated by incubation in 50 mL of Dulbecco's modified Eagle's medium-low glucose (DMEM; 11885-084, Thermo Fisher, MA, USA) containing Active Ingredient type I (210 U mL⁻¹, 17100-017, Thermo Fisher), DNase I (10 μ g mL⁻¹, D4263, Sigma-Aldrich), and Active Ingredient–Active Ingredient (1% w/v, 15140-122, Thermo Fisher) for 2 h at 37 °C with stirring. TMSCs were obtained by filtering the mixture through a cell strainer with 70 μ m pore diameter (93 070, SPL, Seoul, Republic of Korea) and cultured in DMEM supplemented with fetal bovine serum (FBS; 10% w/v, 16000-044, Thermo Fisher) and Active Ingredient–Active Ingredient (1% w/v) by changing culture media every 2 days.

TMSC-derived NVs were produced when TMSCs (passage 3–10) reached 80–90% confluence. TMSCs were detached by treatment with 0.25% trypsin-EDTA (25200-072, Thermo Fisher) for 3 min, followed by

washing with PBS and centrifugation at 1300 rpm for 3 min. The cell suspension underwent serial extrusion in the order of drain disc, 10 µm membrane filters (PTU1009010, Sterlitech), 5 µm membrane filters (PCT509030, Sterlitech), and 0.1 µm membrane filters, and drain disc again in 25 mL min⁻¹ using an extruder and peristaltic pump. Debris was removed with cell collection by centrifugation at 14000 rpm for 30 min, followed by determining the protein concentration of NV using a BCA protein assay kit (23 227, Thermo Fisher).

P. Display onto Liposome and NV: Peptide-attached to polyethylene glycol (pegylated P.) was produced first to display onto liposomes and NV by reacting the NH₂ of P. with DSPE-PEG2000-COOH (880135P, Sigma-Aldrich) at a molar ratio of 1:1 using N-(3-Dimethylaminopropyl)-N-ethylcarbodiimide hydrochloride (E7750, Sigma-Aldrich) with gentle stirring for 24 h at room temperature. Unreacted DSPE-PEG2000-COOH or P. were removed using tubing dialysis (MWCO = 3.5 kDa, G235003, Spectrum Lab, Piraeus, Greece). Then, the pegylated P. (10% w/w) was reacted to display onto the membrane of NV or liposome using the Neon electroporation system (MPK5000, Thermo Fisher) at 1400 V for 2 ms with two pulses. Unreacted pegylated P. was removed by tubing dialysis (MWCO = 20 kDa, G235057, Spectrum Lab), followed by centrifugation at 14000 rpm for 30 min. The targeting efficiency of P. was compared with No. P (pegylation only) and scramble P. with pegylation post electroporation of DSPE-PEG2000-COOH without or with scramble P. to NV. (P. sequence: ACTPSFSKIC, scramble P. sequence: KFTISPSACC—synthesized from LugenSci, Seoul, Republic of Korea)

Characterization of P. NV and P. Liposome: The morphology and size of TMNV, P. NV, and P. liposomes were examined using transmission electron microscopy (Jem2100, JEOL, Tokyo, Japan). Western blotting determined the expression of exosome markers (CD9 and CD63) in TMNV and P. NV (see the corresponding section below for details). Rabbit anti-CD9 (1:1000, ab92726, Abcam, MA, USA), rabbit anti-CD63 (1: 1000, ab231975, Abcam), and mouse anti-actin (1: 1000, sc-47778, Santa Cruz, TX, USA) antibodies were incubated with the samples overnight at 4 °C, followed by incubation with horseradish peroxidase (HRP)-conjugated secondary goat anti-rabbit IgG(H+L) antibodies (1:5000, 31460, Thermo Fisher) or goat anti-mouse IgG(H+L) antibodies (1:5000, 31430, Thermo Fisher).

As a diagnostic signal, X-ray attenuation of Active Ingredient-containing liposomes was determined in Hounsfield units (HU) by comparison with the units of background controls (air and water) and Active Ingredient standards with varying concentrations using DEXA (InAlyzer, Medikors, Gyeonggi, Republic of Korea). FTIR spectroscopy (Nicolet 6700, Thermo Fisher) was used to confirm the PEGylation of P. with major signals at 1765 cm⁻¹ (C=O strong stretching vibration) and then PEGylated P. conjugation to NV or liposomes with sharper bands at 1765 and 1600 cm⁻¹ (C=O and N—H stretching vibration).

Rabbit Model of Allograft Transplantation with Imaging Analysis: The study was approved by the Institutional Animal Care and Use Committee of Yonsei University College of Medicine (2021-0048 for rabbit experiments, 2020-0202 for mouse experiments). Allografts of the common carotid artery were carried out in rabbits (male, 3 kg; New Zealand White, Doo Yeol Biotech, Seoul, Republic of Korea). First, each donor rabbit was sacrificed by IV injection of KCl (10 mEq, Daihan Pharm, Seoul, Republic of Korea) through an ear vein. A common carotid artery (≈3 cm in length) of the donor was cross-clamped and excised for grafting. After washing with PBS, the decellularization process of the donor vessel was performed by pulsatile perfusion of sodium dodecyl sulfate (SDS; 1% w/v in PBS, L3771, Sigma-Aldrich) for 48 h.^[26] The remaining SDS was thoroughly washed out using PBS for 96 h, and the decellularized graft was stored in a lyophilizer (7960041, Labconco, KS, USA).

Each recipient rabbit was anesthetized for grafting by a subcutaneous injection of zoletil (10 mg/kg, Virbac, Seoul, Republic of Korea) and maintained by the endotracheal inhalation of Active Ingredient (Hana Pharm, Gyeonggi, Republic of Korea) in a continuous tube supply. Active Ingredient (100 IU kg⁻¹, JW Pharmaceutical, Seoul, Republic of Korea) was administered intravenously to each recipient rabbit immediately before arterial clamping. Then, an incision (4 cm) was

made into the center of the anterior neck in front of the trachea, followed by dissection of the subcutaneous tissue and neck muscle. A common carotid artery was exposed, both proximal and distal sides were clamped, and the artery between the clamps was excised. The post-decellularized artery (1–2 cm in length) of the donor was inserted for interposition grafting through end-to-end anastomosis using a 9-0 ethilon (2829G, Ethicon, NJ, USA) suture, followed by closing the neck using 5-0 vicryl (W9982, Ethicon) suture. Aspirin (Bayer, Leverkusen, Germany) was administered at a 5 mg/kg dose for 7 days to prevent graft thrombosis.

Immediately after the graft surgery (day 0), blood flow profiles in each case of allograft were characterized using ultrasonography (iU22 xMatrix DS, Philips, Amsterdam, Netherlands). At day 2 post-surgery, P. liposome (500 mg) containing contrast was injected into each rabbit through an ear vein, followed by CT imaging before the liposome injection as well as 0, 24, and 48 h post-injection. CT scanning was performed using a Somatom Sensation 64 channel (Siemens Healthcare, Erlangen, Germany) with image analysis using AquariusNet Viewer (V4.4.13. P6, TeraRecon, NC, USA).

Mouse Model of PCL with Imaging Analysis: Mice underwent PCL as reported previously^[20] using ApoE KO mice (male, 7 weeks old, SLC, Shizuoka, Japan) or Balb/c nude mice (male, 7 weeks old, Orient Bio, Seoul, Republic of Korea). Mice were anesthetized with an intraperitoneal injection of zoletil (50 mg/kg) and xylazine (10 mg/kg, Rompun, Bayer). The midline of the neck was incised to expose the left common carotid artery (LCCA) after shaving and disinfection using povidone-iodine (Green Pharmaceutical, Jincheon, Republic of Korea). Then, three distal branches (internal, external, and occipital artery) of the LCCA were ligated with a 10-0 ethilon (W2814, Ethicon) suture, except the superior thyroid artery, followed by wound closing with 6-0 Vicryl suture (J510G, Ethicon).

At day 3 post ligation, disturbance of blood flow at the LCCA was examined using Doppler ultrasound (Vevo2100, VisualSonics, ON, Canada) under anesthesia with Active Ingredient ApoE KO mice were then fed a high-fat diet (D12079B, Research Diets, NJ, USA). At day 30 post-surgery, P. liposome (200 mg) containing contrast was injected into the tail vein of each mouse, followed by CT imaging before the injection and 0, 24, and 48 h after the injection. CT scanning was performed using Quantum GX2 (Perkin Elmer, MA, USA) with image analysis using AquariusNet Viewer.

Targeting and organ distribution of P. liposomes in each PCL mouse was examined using IVIS (124262, Perkin Elmer) by labeling liposomes with DiI (V22887, Thermo Fisher) followed by tail vein injection at day 3 post PCL. Mice were maintained under Active Ingredient anesthesia to acquire IVIS images (excitation/emission: 644/665 nm wavelength), followed by image analysis using Living Image Software (V4.5.5, Perkin Elmer).

Blood Test to Determine Lipid Accumulation and Liver Function: Mouse and rabbit blood was drawn into a Active Ingredient-coated tube (365 967, BD, NJ, USA) and plasma was separated by centrifugation at 3000× g for 15 min at 4 °C. The levels of LDL, total plasma cholesterol, triglycerides, total bilirubin, aspartate aminotransferase (AST), alanine aminotransferase (ALT), lactate dehydrogenase (LDH), and alkaline phosphatase (ALP) were measured and calculated using an automated clinical chemistry analyzer (FUJI DRI-CHEM NX500i, Fuji Film, Tokyo, Japan).^[27] The NV effects on the liver function in rabbit was examined at day 0 and 14 post vein injection of NV (7.9 mg/rabbit) through the blood test to determine the levels of AST, ALT, LDH, gamma-glutamyl transferase, and ALP.

Anti-Stenotic and Lipid Lowering Effects of P. NV and P. Liposome in PCL Mice: The therapeutic actions of P. NV and P. liposomes were examined with a focus on anti-stenotic and lipid-lowering effects by administering each test group from day 30 post-PCL surgery. While 100 µg of scrambled P. NV or P. NV was injected through the tail vein, daily oral administration was administered to 25 µg of Active Ingredient (JW Pharmaceutical), followed by sacrifice on day 60. Carotid arteries, liver, and aorta were harvested by anesthetizing each mouse with an intraperitoneal injection of zoletil (50 mg/kg) and xylazine (10 mg/kg) mixture. Cold normal saline (10 mL, Daihan Pharm) containing 10%

Active Ingredient was perfused through the left ventricle after cutting the internal vena cava of each mouse to drain the whole blood, followed by harvesting organ tissues.

For paraffin sections, samples were fixed in 10% neutral buffered formalin (F2013, Biosesang, Gyeonggi, Republic of Korea) solution for 24 h and subjected to H&E staining. Immunofluorescence staining was conducted by deparaffinizing and rehydrating the tissue slices, followed by treatment with primary mouse anti-VCAM1 (1:100, c45432, LS Bio, WA, USA), rabbit anti-ICAM1 (1:200, ab179707, Abcam), rabbit anti-CD68 (1:200, ab125212, Abcam), and rabbit anti-CDK9 (1:200, 2316, Cell Signaling, MA, USA) overnight at 4 °C. Samples were subjected to treatment with secondary Alexa Fluor 488 anti-rabbit (1:150, 115-545-003, Jackson Lab, ME, USA) and Alexa Fluor 594 anti-mouse (1:150, 115-585-003, Jackson Lab) antibodies for 1 h.

For frozen sections, tissue samples underwent optimal cutting temperature compound (3801480, Leica Biosystems, IL, USA) embedding, fixed in 4% paraformaldehyde (PFA; CNP015-0500, CellNest, Gyeonggi, Republic of Korea) for 15 min, and permeabilized with blocking in 0.05% Triton X-100 (in PBS; 93443, Sigma-Aldrich) and 1% bovine serum albumin (BSA; 82-100-6, Merck Millipore, MA, USA) for 30 min at room temperature. Treatment of primary antibodies were carried out in 1% BSA buffer containing rabbit anti-IL-6 (1:200, NB600-1131, Novus, CO, USA), rabbit anti-CDK9 (1:200), rabbit anti-BODIPY ROS 581/591 (1:200, D3861, Thermo Fisher) overnight at 4 °C. After washing three times with PBS, the samples were treated with secondary Alexa Fluor 594 anti-rabbit antibodies (1:200) for 1 h at room temperature. All samples were counterstained with DAPI (H1200, Vectashield, Darmstadt, Germany), followed by confocal imaging (LSM980, Carl-Zeiss, Oberkochen, Germany).

Fat deposits in mouse organ tissues were examined by Oil Red O staining (O0625, Sigma-Aldrich) following the supplier's instructions. Mouse liver tissue sections were fixed in 10% neutral buffered formalin for 30 min, dehydrated with propylene glycol (57-55-6, Duksan, Gyeonggi, Republic of Korea), and stained in 0.7% Oil Red O solution with counterstaining of Mayer's hematoxylin (MHS16, Merck Millipore) at 60 °C. Mouse aorta samples were subjected to en face Oil Red O staining at 37 °C for 30 min, followed by immersion in 60% isopropyl alcohol solution (67-63-0, Duksan) and washing with double distilled water. Oil Red O staining of liver sections and aorta was analyzed by optical imaging (DMI8, Leica Microsystems, Wetzlar, Germany). Mouse aorta samples underwent en face staining to examine CDK9 expression after fixing for 40 min in 4% PFA, washing in PBS, permeabilizing with 0.1% Triton X-100 for 10 min, and blocking with 10% normal goat serum (50197Z, Thermo Fisher). The samples were incubated with rabbit anti-CDK9 (1:200) overnight at 4 °C, followed by staining with secondary Alexa Fluor 594 anti-mouse (1:150) antibodies and DAPI. The samples were then subjected to confocal imaging with quantitative image analysis using ImageJ (National Institutes of Health, MD, USA).

Computer Modeling of P. Binding to CDK9 Complex: The binding status of the P. and CDK9 complex (P-TEFb) was computer-modeled by calculating their docking efficiency using the Schrödinger software suite (Schrödinger Release 2021-1: Maestro. Schrödinger, NY, USA). The 3D structure of P-TEFb protein was retrieved from the RCSB Protein Data Bank (PDB; ID of P-TEFb: 3BLQ).^[28] After preprocessing the P-TEFb PDB file with the Protein Preparation Wizard module,^[29] the docking score was analyzed using the Peptide Docking module in the Schrödinger software suite.

Targeting Efficiency of P. in a Flow Model In Vitro: Human aortic endothelial cells (hAECs; passage 3–9, Lonza, Basel, Switzerland) were cultured until confluence on 0.1% gelatin (G1890, Sigma-Aldrich)-coated culture plates using endothelial cell growth medium 2 (EGM-2) supplemented with the EGM-2 Bullet Kit (CC-3162, Lonza) under standard culture conditions. Then, an in vitro flow model was operated by seeding hAECs (5×10^6 cells mL⁻¹) into a customized cone-in-plate until confluence and exposed to laminar versus disturbed flow. After 24 h, the guiding efficiency of P. in targeting disturbed flow sites in the flow model was determined by labeling NV, and liposomes with a DiD fluorescent dye. After hAECs were treated with P. NV-DiD or P. liposome-DiD (25 µg mL⁻¹) and continuously exposed to the flow

conditions for an additional 24 h, the culture medium was removed, and hAECs were washed with PBS to remove unbound P. particles. Next, the samples were fixed with 4% PFA and permeabilized with 0.2% Triton X-100 in PBS, followed by blocking with 5% BSA. CDK9 was immunoblotted with rabbit anti-CDK9 (1:200); actin cytoskeleton was stained with Alexa Fluor 488 Phalloidin (A12379, Thermo Fisher), and nuclei were stained with DAPI in mounting medium. The samples were then subjected to confocal imaging.

Immunoprecipitation: P. binding to the CDK9 complex (P-TEFb) was determined by immunoprecipitation from hAECs after exposure to laminar versus disturbed flow for 24 h and extracting cell proteins using a lysis buffer (ab206996, Abcam). The protein concentration of the cell extract was measured using a BCA protein assay kit, and the input amount of immunoprecipitated protein was determined by western blotting using the extraction protein (25 µg). On the other hand, extract protein (1 mg) was incubated with biotinylated P. (20 µM, LugenSci) at 37 °C for 24 h to allow for binding between P. and CDK9. Biotinylated P.-CDK9 was captured by reacting with Accunano-streptavidin magnetic beads (2 mg, TA-1015-1, Bioneer, Seoul, Republic of Korea) overnight at 4 °C. The magnetic beads with P.-CDK9 were pulled down by placing on a Magliso–Magnetic separation rack (TM-1000, Bioneer), followed by removing the supernatant. The beads were separated from the magnetic rack and washed twice with PBS (0.5 mL). Next, proteins were eluted from magnetic beads by incubating with 2× Laemmli sample buffer (3161-0747, Bio-Rad Laboratories, CA, USA) for 10 min and heating for 10 min at 95 °C, followed by western blot analysis using CDK9 antibodies (sc-484, Santa Cruz).

CDK9 Activity In Vitro: The decremental kinase activity of CDK9 upon binding with P. at incremental concentrations (0–110 µM) was determined using a CDK9 assay kit (79628, BPS Bioscience, CA, USA) according to the manufacturer's instructions. Since the phosphate of ATP is consumed due to phosphorylation of substrate by activation of CDK9/Cyclin T1 kinase, ATP accumulation indicates reduced kinase activity upon P. binding. Hence, P. was reacted with ATP (500 µM), CDK substrate peptide (5×), and CDK9/Cyclin T1 (5 ng µL⁻¹) in 5× kinase buffer at 37 °C for 2 h, followed by addition of Kinase-Glo max reagent (50 µL, V6071, Promega, WI, USA) for 15 min at room temperature in the dark. The ATP amount was quantified by adding Kinase-Glo Plus reagent with reading the luminescence intensity in a luminescent microplate reader (46970, Berthold Technologies, Baden-Württemberg, Germany), followed by normalization to that of the 0 µg P. reaction.

siRNA Knock-Down: Knockdown of CDK9 was induced using siRNA to validate its key roles in targeting and anti-stenotic signaling of P. particles. After exposure to disturbed flow for 24 h, hAECs were treated with siRNA-CDK9 (sc-29268, Santa Cruz) or siRNA-scramble (sc-37007, Santa Cruz) for 24 h under disturbed flow. Lipofectamine RNAiMAX reagent (13778030, Thermo Fisher) was used for cell transfection with incremental siRNA concentrations to determine the working conditions according to the manufacturer's instructions.

qRT PCR: Total RNA was extracted using TRIzol reagent (15596018, Thermo Fisher) following the manufacturer's protocol, and the RNA concentration was measured using a Nanodrop 2000 Spectrophotometer (ND2000, Thermo Fisher). Complementary DNA was synthesized by reverse transcription of 1 µg of RNA using AccuPower CycleScript RT premix (K2044, Bioneer). A real-time PCR system (StepOne V2.3, Applied Biosystems, MA, USA) was run using SYBR green with primers (Table S1, Supporting Information) through 40 cycles of target gene amplification with a holding stage at 95 °C for 10 min, denaturation at 95 °C for 1 min, and annealing at 60 °C for 1 min. The relative expression of each target gene was determined by calculating the $2^{-\Delta\Delta Ct}$ values, and glyceraldehyde 3-phosphate dehydrogenase was used as an internal normalization control.

Western Blot: Total proteins were extracted by treating samples with RIPA buffer (R0278, Sigma-Aldrich) on ice, followed by centrifugation at 13200 rpm for 30 min. After measuring the protein concentration using a BCA protein assay kit, proteins (25 µg) were separated on a 10% SDS-polyacrylamide Mini-Protein TGX gels (456-1094, Bio-Rad Laboratories) and electrotransferred onto a nitrocellulose membrane using iBlot 2 NC

gel regular stacks (2NR 111018-01, Thermo Fisher). The membrane was blocked in 1× Tris-buffered saline buffer (TBST; BTT-9110, T&L, Seoul, Republic of Korea) with 5% non-fat dry skim milk (1706404, Bio-Rad Laboratories) containing 0.1% tween-20 (P9416, Sigma-Aldrich) for 1 h at room temperature. The membranes were incubated with primary mouse anti-VCAM1 (1:1000), rabbit anti-CD68 (1:200), rabbit anti-CDK9 (1: 1000), rabbit anti-IL-8 (1:100, NBP2-33819, Novus), rabbit anti-IL-1 β (1:100, NB600-633, Novus), rabbit anti-CD9 (1:100), rabbit anti-CD63 (1:1000), and mouse anti-actin (1: 1000) antibodies after dilution in 5% skim milk TBST at 4 °C overnight. Then, the membranes were washed with 1× TBST three times (each for 15 min) and incubated with secondary goat anti-rabbit IgG(H+L)-HRP conjugated (1: 5000) or goat anti-mouse IgG(H+L)-HRP conjugated (1: 5000) antibodies for 1 h. After washing three times with 1× TBST, the blot signals were visualized using a western ECL substrate (170-5060, Bio-Rad Laboratories) according to the manufacturer's instructions and analyzed using LAS-3000 (Fuji Film), followed by quantitative analysis with normalization to the intensity of actin.

Statistical Analysis: All statistical analyses were performed using Excel and SigmaPlot (V12.0, Systat Software, CA, USA). Data are presented as the mean \pm standard error of the mean (SEM) based on more than three independent experiments. The significance of the differences between the two groups was determined using a two-tailed Student's *t*-test. Multiple comparisons among test groups were conducted using one-way analysis of variance, followed by post-hoc Bonferroni's analysis. Statistical significance was set at $p < 0.05$. The size of biologically independent samples per group and/or the number of independent experiments are denoted in each figure and legend.

Supporting Information

Supporting Information is available from the Wiley Online Library or from the author.

Acknowledgements

The Korean government grants include i) the Korea Medical Device Development Fund, supported by Ministry of Science and ICT, the Ministry of Trade, Industry and Energy, Ministry of Health & Welfare, and Ministry of Food and Drug Safety (Project Number: 1711138302, KMDF_PR_20200901_0152); ii) the Bio & Medical Technology Development Program of the National Research Foundation (NRF) (2019R1A2C2010802-HJS, 2020R1C1C1010579-SEY), and iii) the MD-PhD/Medical Scientist Training Program through the Korea Health Industry Development Institute (KHIDI), funded by the Ministry of Health & Welfare.

Conflict of Interest

The authors declare no conflict of interest.

Author Contributions

S.E.Y. and S.C. contributed equally to this work as co-first authors. C.-S.K. and H.-J.S. (Lead) are listed as the co-corresponding authors, considering their significant contributions. H.-J.S. designed and directed the entire study. S.E.Y. and S.C. led the experiments, analyzed the data, and prepared the figures and tables. S.B., T.Y.K., H.S.K., and S.Y.K. collaborated on the in vitro studies, and H.-S.H., D.-H.K., S.H.L, H.-J.Y., S.-W.C. assisted in the animal studies. J.B.L. and Y.M.S. contributed to the experimental design. Computer modeling analyses were conducted by J.-S.P. H.-J.S. drafted the manuscript with assistance from S.E.Y. and S.C.

Data Availability Statement

The data that support the findings of this study are available from the corresponding author upon reasonable request.

Keywords

CDK9, disturbed flow, nanotheranostics, pre-stenotic vessel, targeting peptide

Received: October 13, 2021

Revised: November 23, 2021

Published online: December 8, 2021

- [1] V. J. Dzau, R. C. Braun-Dullaeus, D. G. Sedding, *Nat. Med.* **2002**, *8*, 1249.
- [2] K. Ley, C. Laudanna, M. I. Cybulsky, S. Nourshargh, *Nat. Rev. Immunol.* **2007**, *7*, 678.
- [3] R. M. Rao, L. Yang, G. Garcia-Cardena, F. W. Lusinskas, *Circ. Res.* **2007**, *101*, 234.
- [4] P. Libby, P. M. Ridker, G. K. Hansson, *Nature* **2011**, *473*, 317.
- [5] Authors/Task Force Members, ESC Committee for Practice Guidelines (CPG), ESC National Cardiac Societies, *Atherosclerosis* **2019**, *290*, 140.
- [6] J.-J. Chiu, S. Chien, *Physiol. Rev.* **2011**, *91*, 327.
- [7] P. Libby, G. Pasterkamp, F. Crea, I. K. Jang, *Circ. Res.* **2019**, *124*, 150.
- [8] L. H. Hofmeister, S. H. Lee, A. E. Norlander, K. R. C. Montaniel, W. Chen, D. G. Harrison, H.-J. Sung, *ACS Nano* **2015**, *9*, 4435.
- [9] M. Barboric, R. M. Nissen, S. Kanazawa, N. Jabrane-Ferrat, B. M. Peterlin, *Mol. Cell* **2001**, *8*, 327.
- [10] Y. Han, S. Zhao, Y. Gong, G. Hou, X. Li, L. Li, *Oncotarget* **2016**, *7*, 1854.
- [11] X. He, Z. Lian, Y. Yang, Z. Wang, X. Fu, Y. Liu, M. Li, J. Tian, T. Yu, H. Xin, *Mol. Ther.–Nucleic Acids* **2020**, *22*, 84.
- [12] X. Yang, W. Luo, L. Li, X. Hu, M. Xu, Y. Wang, J. Feng, J. Qian, X. Guan, Y. Zhao, G. Liang, *Toxicol. Appl. Pharmacol.* **2021**, *416*, 115465.
- [13] A. Hellvard, L. Zeitlmann, U. Heiser, A. Kehlen, A. Niestroj, H. U. Demuth, J. Koziel, N. Delaleu, P. Jan, P. Mydel, *Sci. Rep.* **2016**, *6*, 31441.
- [14] M. B. Miranda, K. F. Dyer, J. R. Grandis, D. E. Johnson, *Leukemia* **2003**, *17*, 390.
- [15] U. K. Schmerwitz, G. Sass, A. G. Khandoga, J. Joore, B. A. Mayer, N. Berberich, F. Totzke, F. Krombach, G. Tiegs, S. Zahler, A. M. Vollmar, R. Furst, *Arterioscler., Thromb., Vasc. Biol.* **2011**, *31*, 280.
- [16] C. Pang, G. Huang, K. Luo, Y. Dong, F. He, G. Du, M. Xiao, W. Cai, *Cancer Med.* **2017**, *6*, 2398.
- [17] G. Qiu, G. Zheng, M. Ge, J. Wang, R. Huang, Q. Shu, J. Xu, *Stem Cell Res. Ther.* **2018**, *9*, 320.
- [18] J. Key, J. F. Leary, *Int. J. Nanomed.* **2014**, *9*, 711.
- [19] D. P. Cormode, P. C. Naha, Z. A. Fayad, *Contrast Media Mol. Imaging* **2014**, *9*, 37.
- [20] J.-K. Yoon, D.-H. Kim, M.-L. Kang, H.-K. Jang, H.-J. Park, J. B. Lee, S. W. Yi, H.-S. Kim, S. Baek, D. B. Park, J. You, S.-D. Lee, Y. Sei, S. I. Ahn, Y. M. Shin, C. S. Kim, S. Bae, Y. Kim, H.-J. Sung, *Small* **2020**, *16*, 2000012.
- [21] F. R. Maxfield, I. Tabas, *Nature* **2005**, *438*, 612.
- [22] I. Tabas, *J. Clin. Invest.* **2002**, *110*, 905.
- [23] S. Wang, P. M. Fischer, *Trends Pharmacol. Sci.* **2008**, *29*, 302.
- [24] F. K. Swirski, M. Nahrendorf, M. Etzrodt, M. Wildgruber, V. Cortez-Retamozo, P. Panizzi, J. L. Figueiredo, R. H. Kohler, A. Chudnovskiy, P. Waterman, E. Aikawa, T. R. Mempel, P. Libby, R. Weissleder, M. J. Pittet, *Science* **2009**, *325*, 612.

- [25] C. S. Robbins, A. Chudnovskiy, P. J. Rauch, J. L. Figueiredo, Y. Iwamoto, R. Gorbatov, M. Etzrodt, G. F. Weber, T. Ueno, N. van Rooijen, M. J. Mulligan-Kehoe, P. Libby, M. Nahrendorf, M. J. Pittet, R. Weissleder, F. K. Swirski, *Circulation* **2012**, *125*, 364.
- [26] J. S. Lee, Y. H. Roh, Y. S. Choi, Y. Jin, E. J. Jeon, K. W. Bong, S. W. Cho, *Adv. Funct. Mater.* **2019**, *29*, 1807909.
- [27] W. T. Friedewald, R. I. Levy, D. S. Fredrickson, *Clin. Chem.* **1972**, *18*, 499.
- [28] H. M. Berman, J. Westbrook, Z. Feng, G. Gilliland, T. N. Bhat, H. Weissig, I. N. Shindyalov, P. E. Bourne, *Nucleic Acids Res.* **2000**, *28*, 235.
- [29] I. Tubert-Brohman, W. Sherman, M. Repasky, T. Beuming, *J. Chem. Inf. Model.* **2013**, *53*, 1689.